Terahertz radiation as a bunch diagnostic for laser-wakefield-accelerated electron bunches[a)]

J. van Tilborg[b)] and C. B. Schroeder
Lawrence Berkeley National Laboratory, University of California, Berkeley, California 94720

C. V. Filip
University of Nevada, Reno, Nevada 89557

Cs. Tóth, C. G. R. Geddes, and G. Fubiani[c)]
Lawrence Berkeley National Laboratory, University of California, Berkeley, California 94720

E. Esarey and W. P. Leemans
Lawrence Berkeley National Laboratory, University of California, Berkeley, California 94720
and University of Nevada, Reno, Nevada 89557

(Received 29 October 2005; accepted 27 February 2006; published online 11 May 2006)

DISCLAIMER

Terahertz radiation as a bunch diagnostic for laser-wakefield-accelerated electron bunches[a)]

J. van Tilborg[b)] and C. B. Schroeder
Lawrence Berkeley National Laboratory, University of California, Berkeley, California 94720

C. V. Filip
University of Nevada, Reno, Nevada 89557

Cs. Tóth, C. G. R. Geddes, and G. Fubiani[c)]
Lawrence Berkeley National Laboratory, University of California, Berkeley, California 94720

E. Esarey and W. P. Leemans
Lawrence Berkeley National Laboratory, University of California, Berkeley, California 94720 and University of Nevada, Reno, Nevada 89557

(Received 29 October 2005; accepted 27 February 2006; published online 11 May 2006)

Experimental results are reported from two measurement techniques (semiconductor switching and electro-optic sampling) that allow temporal characterization of electron bunches produced by a laser-driven plasma-based accelerator. As femtosecond electron bunches exit the plasma-vacuum interface, coherent transition radiation (at THz frequencies) is emitted. Measuring the properties of this radiation allows characterization of the electron bunches. Theoretical work on the emission mechanism is presented, including a model that calculates the THz wave form from a given bunch profile. It is found that the spectrum of the THz pulse is coherent up to the 200 μm thick crystal (ZnTe) detection limit of 4 THz, which corresponds to the production of sub-50 fs (rms) electron bunch structure. The measurements demonstrate both the shot-to-shot stability of bunch parameters that are critical to THz emission (such as total charge and bunch length), as well as femtosecond synchronization among bunch, THz pulse, and laser beam. © *2006 American Institute of Physics*.
[DOI: 10.1063/1.2187957]

I. INTRODUCTION

Laser-wakefield accelerators[1–9] (LWFAs) have recently gained interest because of their ability to produce relativistic electrons,[3–9] THz radiation,[10–14] x-rays,[15–17] and gamma-ray photons,[18] all intrinsically synchronized in time (on the femtosecond time scale) with the laser pulse. The acceleration mechanism is based on the nonlinear interaction of a near-infrared (NIR) laser pulse (intensity $>10^{19}$ W cm^{-2}) with a plasma (density $\sim 10^{19}$ cm^{-3}). Relativistic electron bunches, containing several nanocoulombs of charge, with a length on the order of the plasma wavelength ($\sim 5-30$ μm), and a transverse size on the order of the laser spot size ($\sim 5-20$ μm) are predicted[19,20] to be produced. Although parameters such as charge and electron energy have been experimentally confirmed,[3–9] temporal characterization of the short bunch has been limited.[10,21]

For conventional accelerators, bunch characterization is typically done with two independent techniques. One (more recent) technique relies on directly measuring the Coulomb field of the bunch through electro-optic sampling.[22–26] Another technique relies on the spectral characterization of coherent radiation (typically through interferometry), emitted by an electron bunch after it propagates through a discontinuity in a dielectric environment. The discontinuity can be realized through insertion of a metallic foil in the bunch path,[27–29] resulting in the emission of coherent transition radiation (CTR).[30] To implement a diagnostic for LWFA-produced bunches, we rely on the emission of CTR (predominantly at THz frequencies), emitted as the electron bunch exits the plasma-vacuum interface. In recent years, the existence of THz (CTR) emission from the LWFA has been experimentally confirmed and reported.[10,12,14] Section II provides an overview of theoretical understanding of LWFA-produced CTR.

To date, CTR-based LWFA-bunch analysis was performed in only one experiment, where total THz energy was measured in two spectral regimes[10] (suggesting sub-100 fs bunch structure). In order to provide more detailed bunch and THz profile analysis (including possible profile asymmetries or multipulse structures), we report in this publication on two techniques applied for temporal characterization of the THz pulse, both with use of a NIR laser pulse. All experiments discussed in this paper were performed at a plasma density of $\simeq 3\times 10^{19}$ cm^{-3}. At such high densities, the acceleration scheme is referred to as the self-modulated LWFA (SM-LWFA), since the laser pulse length is longer than the plasma wavelength (which results in a laser envelope modulation at the plasma wavelength). Section III presents the first measurement technique, semiconductor switching (SCS),[31–33] where the NIR pulse serves as a pump and the THz pulse as a probe beam. SCS is suitable for THz enve-

[a)]Paper FI2 4, Bull. Am. Phys. Soc. **50**, 105 (2005).
[b)]Invited speaker. Also at Eindhoven University of Technology, the Netherlands.
[c)]Also at University of Paris XI, Orsay, France.

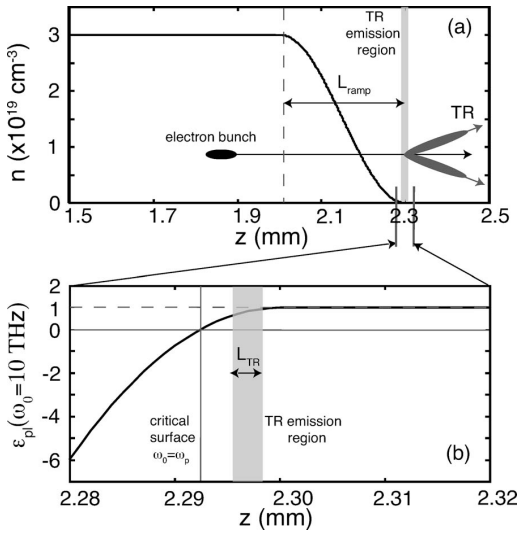

FIG. 1. (a) Longitudinal plasma density profile $n(z)$. (b) The spatially varying dielectric constant $\epsilon_{\rm pl}(z,\omega_0)$ for TR of frequency $\omega_0=10$ THz. The electron bunch is propagating from left to right.

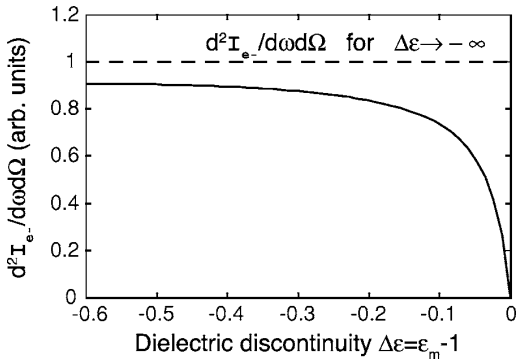

FIG. 2. The differential energy distribution $d^2I_{e^-}/d\omega d\Omega$ (solid curve) for an electron passing the dielectric discontinuity of the medium-vacuum interface ($\epsilon=\epsilon_m$ to $\epsilon=1$), with $\Delta\epsilon=\epsilon_m-1$. The dashed line represents $d^2I_{e^-}/d\omega d\Omega$ in the (metal-vacuum) limit of $\Delta\epsilon\rightarrow-\infty$.

lope characterization as well as establishment of THz-to-NIR synchronization. Section IV presents the second technique, electro-optic sampling (EOS),[22–26,34–36] where the THz pulse serves as the pump and the NIR pulse as the probe beam. EOS allows for the measurement of the THz electric field profile (amplitude and phase). Section V discusses the results in terms of bunch and THz profile reconstruction. Both techniques require shot-to-shot stability of bunch parameters that are critical to THz emission and detection such as total charge, bunch length, and temporal synchronization. Since multiple ultrashort beams are involved, the measurements prove applicability of the SM-LWFA in pump-probe experiments.

II. THEORY: THz RADIATION FROM THE LASER-WAKEFIELD ACCELERATOR

A. The plasma-vacuum boundary as THz emitter

The dielectric function in a (cold) plasma is given by $\epsilon_{\rm pl}(\omega)=1-\omega_p^2/\omega^2$, with ω_p the plasma (angular) frequency related to plasma density n through $\omega_p\,[\mathrm{s}^{-1}]=5.64\times10^4\sqrt{n\,[\mathrm{cm}^{-3}]}$. The longitudinal plasma profile in LWFA experiments is nonuniform, as determined by the gas emission profile, and follows the density function $n(z)$, with z the propagation direction of the laser. It is for this reason that the dielectric function also has a spatial dependence $\epsilon_{\rm pl}(\omega,z)$, resulting in the emission of transition radiation (TR) if an electron bunch passes through. We next present a heuristic picture for the location in the plasma where the TR is emitted, and at what intensity compared to TR from a metal-vacuum boundary.

We define a density profile as plotted in Fig. 1(a), which is characteristic for the experiments described in this publication. Density interferometry has confirmed the agreement between modeled and actual profile. The transverse size of the plasma is on the order of 100–300 μm. The density interferometer is less sensitive at low plasma densities ($n<10^{18}$ cm^{-3}), and plasma parameters in this regime are therefore based on estimations. Figure 1(a) shows a uniform density profile (up to $z=2$ mm and starting at $z=0$ mm), followed by a down ramp with length $L_{\rm ramp}$, which has a length on the order of $\simeq300$ μm. We focus now on TR with frequency $\omega_0=10$ THz, although TR at any arbitrary radiation frequency can be analyzed in a similar manner. For $\omega_0=10$ THz, one can derive the spatially varying dielectric constant $\epsilon_{\rm pl}(z,\omega_0)$, plotted in Fig. 1(b). Note that the z range in Fig. 1(b) is only a small fraction of the z range in Fig. 1(a). In the high-density region ($n\approx10^{17}-10^{19}$ cm^{-3}), the density is highly overcritical for ω_0 such that $\epsilon_{\rm pl}(\omega_0)\rightarrow-\infty$. Only in the lower-density part of the ramp ($n\lesssim10^{17}$ cm^{-3}) does the dielectric constant reach positive values, and eventually becomes $\epsilon=1$ in vacuum.

Before continuing the discussion on the location in the plasma profile where the TR is emitted, we will take a necessary step back and consider TR from a step boundary between a medium with dielectric constant $\epsilon=\epsilon_m$ and vacuum ($\epsilon=1$). The following expression for the radiated energy $d^2I_{e^-}$ per unit bandwidth $d\omega$ and unit solid angle $d\Omega$ can be found in the literature:[30]

$$\frac{d^2I_{e^-}}{d\omega d\Omega}=\frac{e^2}{\pi^2c}\left[\frac{\epsilon_m-1}{(1-\beta^2\cos^2\theta)(1-\beta\sqrt{\epsilon_m-\sin^2\theta})}\right]^2\times\left[\frac{1-\beta^2-\beta\sqrt{\epsilon_m-\sin^2\theta}}{\sqrt{\epsilon_m-\sin^2\theta}+\epsilon_m\cos\theta}\right]^2,\qquad(1)$$

with $\beta=v/c$, the velocity v of the electron normalized to the speed of light c, θ the angle of observation measured with respect to the z axis, and e the unit electron charge. Note that this expression is only valid for a single electron propagating along the z axis at normal incidence to the interface. In Fig. 2, one can see (solid curve) the dependency of $d^2I_{e^-}/d\omega d\Omega$ on $\Delta\epsilon=\epsilon_m-1$, with values for ϵ_m in the range of 0.4–1. For this calculation we used $\theta=0.15$ rad, and $u=10$, with $u=\beta/\sqrt{1-\beta^2}$ the electron momentum normalized to m_ec. The dashed line corresponds to the differential energy emitted for

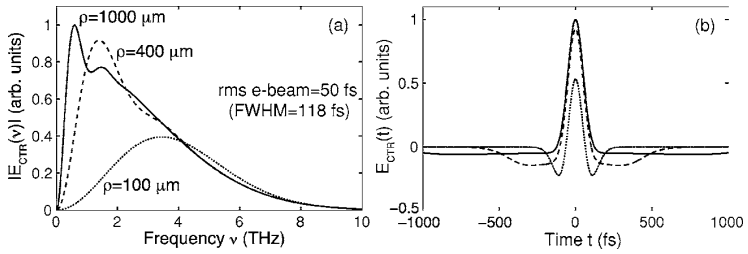

FIG. 3. The amplitude of the CTR electric field in the (a) Fourier domain $|E_{\mathrm{CTR}}(\nu)|$ and in the (b) temporal domain $E_{\mathrm{CTR}}(t)$, calculated for an interface with boundary radius $\rho=1000$ μm (solid line), $\rho=400$ μm (dashed line), and $\rho=100$ μm (dotted line). The rms bunch length is 50 fs, the electron momentum is $u=10$, and the angle of observation is $\theta=0.3$ rad.

the (metal-vacuum) discontinuity, where $\epsilon_m \to -\infty$. One can see that the transition $\Delta\epsilon=-0.2$ ($\epsilon_m=0.8$) results in nearly 90% of the radiation emission compared to $\Delta\epsilon=-\infty$. This indicates that TR emission is dominated by the $\epsilon=0.8\to1$ boundary (the transition $\epsilon=-\infty\to0.8$ will result in emission of only a fraction of the energy of the $\epsilon=0.8\to1$ interface).

We return now to TR from the plasma profile in Fig. 1(a). When the electron bunch propagates through the density ramp, and passes through a change in dielectric constant from $\epsilon_{\mathrm{pl}}=-\infty$ to $\epsilon=1$, the TR emission occurs predominantly at the very end of the ramp, where $\epsilon_{\mathrm{pl}}\simeq0.8$. Although the transition $\epsilon_{\mathrm{pl}}\simeq0.8\to1$ is not a step boundary, but a region with width L_{TR}, it can been shown that the emission region is still well modeled as a step boundary,[37] provided L_{TR} is smaller than the formation length L_{form}, given by $L_{\mathrm{form}}=\lambda/(2-2\beta\cos\theta)$, with λ the radiation wavelength and $\beta=v/c$ the normalized velocity of the electron. Although the expression for L_{form} is derived for a vacuum environment, it holds in the underdense region of the plasma. For typical SM-LWFA parameters, the radiation frequencies of interest are in the THz regime, θ is typically on the order of 0–0.3 rad, and the electrons in the bunch contributing to the TR have $\gamma\gtrsim4$. One can find that for these parameters $L_{\mathrm{form}}\gtrsim0.3$ cm. Since $L_{\mathrm{TR}}\ll100$ μm, the step-boundary approximation is indeed valid. The position of the emission region (approximated as a plane) is drawn in Figs. 1(a) and 1(b).

B. Radiated field and intensity distribution for coherent transition radiation

Section II A discussed the emission of TR by a single electron propagating through a plasma-vacuum interface. It was shown that the plasma-vacuum boundary can be approximated by a metal-vacuum step boundary. In this case, Eq. (1) can be simplified to

$$\frac{d^2I_{e^-}}{d\omega d\Omega}=\frac{e^2}{\pi^2c}\varepsilon^2,\quad \text{with } \varepsilon(u)=\frac{u\sqrt{1+u^2}\sin\theta}{1+u^2\sin^2\theta}. \tag{2}$$

We will now include both coherent effects, which refers to the TR emission of a collection of electrons (CTR), as well as diffraction effects due to the finite transverse dimension of the boundary. The electrons are bunched according to their temporal charge distribution $Q(t)$. The angular and spectral intensity distribution of CTR is given by[11]

$$\frac{d^2I_{\mathrm{CTR}}}{d\omega d\Omega}=\frac{e^2N^2}{\pi^2c}\left|\int g(u)\varepsilon(u)D(\omega,u)F(\omega)du\right|^2, \tag{3}$$

with N the number of electrons in the bunch, and $g(u)$ the electron momentum distribution. In this equation, $F(\omega)$ stands for the form factor, given by the Fourier transform of $Q(t)$, or $F(\omega)=\int Q(t)\exp(-\imath\omega t)dt$. It is assumed that the transverse bunch size is smaller than the longitudinal length and that the electrons are relativistic. The electron momentum distribution is assumed to be uncorrelated in time or position. The diffraction function $D(\omega,u)$ is given by[11]

$$D(\omega,u)=1-J_0(bu\sin\theta)\left[bK_1(b)+\frac{1}{2}b^2K_0(b)\right]-\frac{1}{2}b^2K_0(b)J_2(bu\sin\theta), \tag{4}$$

with $b=\omega\rho/(uc)$, ρ the transverse radius of the emission plane, and J_m and K_m the mth-order regular and modified Bessel functions, respectively.

Van Tilborg *et al.*[13] extended the above CTR analysis to derive expressions for the electric field wave form rather than the intensity distribution. The (complex) electric field in the frequency domain was found to be expressed as

$$E_{\mathrm{CTR}}(\omega,R)=\frac{2eN}{cR}e^{-i\omega R/c}\int\varepsilon(u)D(\omega,u)F(\omega)g(u)du, \tag{5}$$

with R the distance to the observation point. The temporal profile of the CTR electric field wave form is given by $E_{\mathrm{CTR}}(t,R)=1/(2\pi)\int E_{\mathrm{CTR}}(\omega,R)e^{i\omega t}d\omega$. It was shown[13] that the solution to Eq. (5) for a mono-energetic bunch at u_t does not significantly differ from the solution for a Boltzmann-like momentum distribution $[\sim\exp(-u/u_t)]$ with temperature u_t. Figure 3 shows, for a mono-energetic electron bunch ($u=10$) with a 50 fs (rms) pulse length, the THz electric field profiles in the temporal and Fourier domains (with $\omega=2\pi\nu$) for various values for the transverse boundary size ρ. The angle of observation is set at $\theta=0.3$ rad. The solid curve is calculated with $\rho=1000$ μm, the dashed curve with $\rho=400$ μm, and the dotted curve with $\rho=100$ μm. The THz pulse can be described as a broad-bandwidth and single-cycle wave form. As Fig. 3 illustrates, the effects of a decreasing boundary size are (i) to remove the lower frequencies for $|E_{\mathrm{CTR}}(\nu)|$, and (ii) to bring the negative side-wings in the temporal wave form $E_{\mathrm{THz}}(t)$ closer together at larger amplitude.

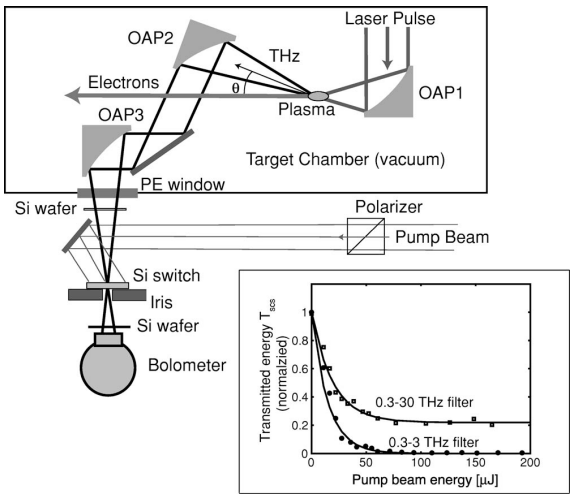

FIG. 4. Schematic representation of the setup for semiconductor switching of LWFA-produced THz radiation. The THz pulse is produced in the vacuum chamber by an ultra-intense laser pulse. A second laser beam (pump beam) provides the switching at the Si wafer. The inset displays the change in THz transmission T_{SCS} (through the Si) as a function of pump beam energy for 0.3–3 THz (circles) and 0.3–30 THz (squares) bolometer filtration.

III. EXPERIMENT: SEMICONDUCTOR SWITCHING

A. Configuration and model for THz switching

One technique that provides temporal insight into the THz radiation pulse is the technique referred to as semiconductor switching.[31] The technique has been applied since the 1970s, and was (among others) used for short-pulse production of CO_2 laser pulses.[32,33] The principle of SCS is that a pump beam excites a dense electron-hole plasma (free carriers) at the surface of a semiconductor. The pump beam can be either an electron beam, or (such as in this experiment) a laser beam at a central frequency above the band gap of the semiconductor. The excitation is almost instantaneous (less then a few femtoseconds), although it will remain for many picoseconds. The excitation switches the semiconductor properties from transmissive to reflective regarding THz pulses. The SCS experiment was performed to establish temporal synchronization between the THz pulse and the NIR laser beam (crucial for the EOS experiment described in Sec. IV), and to provide insight in the envelope profile of the THz pulse. However, this technique is not well suited for detailed bunch characterization.

The setup for SCS is sketched in Fig. 4. A $Ti:Al_2O_3$ laser beam (wavelength of $\lambda_0=800$ nm) was focused [spot size $\simeq 3.6$ μm (rms)] by an off-axis parabola (OAP1) onto helium gas emerging from a gas jet (diameter of 2 mm) with a backing pressure of 1000 psi. The peak electron density in the plasma was 3×10^{19} cm^{-3}, corresponding to a plasma wavelength of $\lambda_p=6$ μm. The laser pulse length was 50 fs [full width at half-maximum (FWHM)], which is about 2.5 times longer than λ_p, such that the accelerator is operated in the regime of SM-LWFA. The laser system was clean of prepulses at intensities $\gtrsim 10^{14}$ W cm^{-2}, as verified with a (femtosecond) plasma density interferometry technique.

The charge of the electron bunch was $\simeq 2.4$ nC, measured 50 cm from the gas jet. The electron momentum distribution $g(u)$, measured by an imaging magnetic spectrometer and averaged over multiple shots, showed an exponential form $\exp(-u/u_t)$ with temperature $u_t=10$. During another experiment[12] with the same laser system, the transverse charge distribution was measured using a phosphor plate at 75 cm from the gas jet. The data indicated fluctuations in divergence ranging from 10–100 mrad; over this range the beam can be approximated as divergenceless in terms of THz emission, as discussed in Ref. 11. Details on measurement of the electron charge, energy distribution, and beam divergence were described in Ref. 12.

Part of the THz radiation was collected and collimated by an $F/2$ 90°-off-axis parabola (OAP2, 15 cm focal length), positioned off-center ($\theta=19^\circ$ with respect to the main propagation axis) to avoid damage from the electron or laser beams. The half-opening angle for OAP2 was $\simeq 15^\circ$. The collimated THz radiation was then focused by an $F/2.4$ 90°-off-axis parabola (OAP3, 18 cm focal length) onto a high-resistivity $\langle 111\rangle$ silicon wafer (serving as Si switch), with a thickness of 0.6 mm [a 3.2 mm thick polyethylene disk served as vacuum window]. An iris was positioned at the THz focal plane just behind the Si switch and had an opening diameter of 1.6 mm. At a distance of 2 cm, a liquid-helium-cooled detector (SiC bolometer) measured the incident THz radiation energy. Two internal filters in the bolometer allowed the user to select a 0.3–3 THz or 0.3–30 THz spectral acceptance. Several other Si wafers were positioned in the THz beam path to block low-intensity remnant laser light. Also incident on the Si switch was a collimated $Ti:Al_2O_3$ laser beam, used as the pump beam for the excitation of free carriers at the Si surface. The spot size was 3.0 mm (FWHM) and the pulse length was 60 fs (FWHM). The angle of incidence of the pump beam with respect to the normal of the Si surface was 12°. The timing τ between THz pulse and laser beam was varied with a delay stage.

A heuristic model of SCS is presented here. The transmission T_{SCS} of a specific THz time slice P_{THz} $(t\rightarrow t+dt)$ depends on the cumulative pump energy $W_p^*(t)$ that has arrived prior to this time slice, or $T_{SCS}=T_{SCS}(W_p^*)$. $P=|E|^2$ refers to the power. The transmission function $T_{SCS}(W_p^*)$ can be experimentally determined by delaying the entire THz pulse (such that the pump beam arrives at the Si first) and recording transmitted THz energy as a function of pump beam energy. The inset in Fig. 4 displays the measured transmission curve for 0.3–3 THz filtration (bottom curve, circles) and 0.3–30 THz filtration (top curve, squares). Exponential fits to the curves yielded $\alpha=0.069$ μJ^{-1} (0.3–3 THz filter) and $\alpha=0.051$ μJ^{-1} (0.3–30 THz filter), with $T_{SCS}\sim\exp(-\alpha W_p)$ and W_p in units of μJ. In the case of the 0.3–30 THz spectral acceptance, one can see that the switch is not perfect, since 22% of the THz energy leaks through the switch regardless of pump beam timing and energy. We suggest that a cutoff frequency exists, above which the laser-induced semiconductor plasma is ineffective in reflecting the radia-

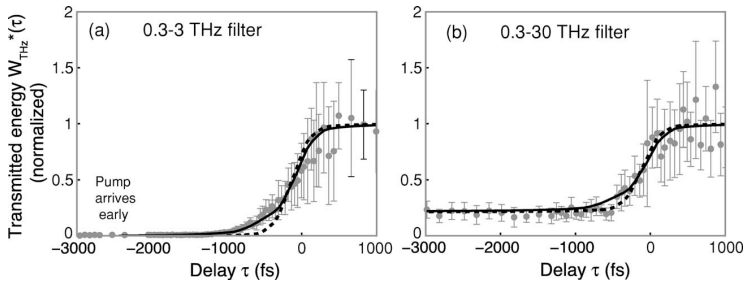

FIG. 5. The measured THz energy transmission versus time delay τ: (a) 0.3–3 THz bolometer filtration and a pump beam energy of 195 μJ and (b) 0.3–30 THz filtration and a pump energy of 180 μJ. Both (a) and (b) also display modeled transmission curves based on (dashed curve) THz from a single 50 fs (rms) electron bunch (single THz pulse) and based on (solid curve) a double-pulse THz profile, with the pulses separated by 300 fs and the leading pulse having a 50% relative field amplitude. Each THz pulse is based on CTR from a bunch with rms length of 50 fs.

tion. With $T_{\mathrm{SCS}}(W_p^*)$ experimentally characterized, the total THz pulse energy $W_{\mathrm{THz}}^*(\tau)$ (after the passing through the switch) can be expressed as

$$W_{\mathrm{THz}}^*(\tau) = \int_{-\infty}^{\infty} P_{\mathrm{THz}}(t-\tau) T_{\mathrm{SCS}}\left[W_p^* = \int_{-\infty}^{t} P_p(t')dt' \right] dt. \tag{6}$$

In the limit of an ultrashort pump beam $P_{\mathrm{p}}(t)$, Eq. (6) reduces to $W_{\mathrm{THz}}^*(\tau) = \int_{-\infty}^{-\tau} P_{\mathrm{THz}}(t)dt$.

B. Experimental results for THz switching

The measured bolometer energy at various values for pump-beam time delay τ is shown for two separate scans in Figs. 5(a) and 5(b). Each data point represents an average of 30 shots (typically at 1 Hz repetition) and the error bars represent the rms spread. Figure 5(a) displays a scan taken with the bolometer at 0.3–3 THz filtration, and pump beam energy of 195 μJ (or 9.2×10^{10} $W\,\mathrm{cm}^{-2}$). Figure 5(b) displays a scan with 0.3–30 THz filtration and 180 μJ of pump energy. When comparing to a model, the data do not allow for detailed insight on the charge profile. However, the THz pulse envelope is found to have a (rms) length $<$400 fs.

Theoretical predicted transmission curves [from Eqs. (5) and (6)], based on two different THz pulse profiles, were calculated. The noncollinear geometry between THz and pump pulse (see Fig. 4) is taken into account by assuming a THz spot size of 0.5 mm (FWHM). The dashed curve in Figs. 5(a) and 5(b) indicates the modeled transmitted energy profile for THz from a Gaussian electron beam, with a rms length of 50 fs (single THz pulse). The solid curve represents THz transmission from a double-pulse THz profile (see discussion in Sec. V); the pulses are separated by 300 fs, with the leading pulse having a 50% relative field amplitude, and each THz pulse is calculated from a 50 fs (rms) electron bunch. Both solid and dashed curves capture the features of the measurement, with a slight preference for the model based on the double-pulse THz profile [see Fig. 5(a)]. Note that if just one longer single-cycle THz pulse was assumed for the model (rms length of 400 fs), its modeled transmission curve would also match the data of Figs. 5(a) and 5(b). However, it would be contradictory to previously obtained energy measurements that clearly indicate that a significant amount of THz energy (more than 70%) is at frequencies above 3 THz.[12] One longer single-cycle pulse would not contain spectral components above 3 THz, indicating that a more complicated (double pulse) THz profile was present in the focal volume (confirmed by EOS data in Sec. IV B).

IV. EXPERIMENT: ELECTRO-OPTIC SAMPLING

A. Configuration and model for electro-optic sampling

In contrast to the SCS experiment, the EOS technique is able to resolve both the phase and amplitude of the THz wave form. The setup for EOS is sketched in Fig. 6. The arrangement of THz optics inside the target chamber is identical to the SCS experiments and can be found in Fig. 4 with explanatory comments in Sec. III A. The THz pulse, coming out of the target chamber, is focused onto a thin electro-optic (EO) crystal. An ultrashort NIR laser beam was used to probe the THz-induced change in crystal birefringence. By scanning the delay between both pulses, a full THz wave form was measured. A polarizer ensured horizontal polarization of the probe beam, and a $\lambda/4$ plate was used to modify the probe beam polarization incident on the analyzer. The analyzer was set to transmit the vertical component to diode 1, and the horizontal component to diode 2. The electric field vectors of the probe beam and THz pulse are shown in the inset of Fig. 6. Although the emitted THz pulse is radially polarized coming from the plasma-vacuum interface,[11]

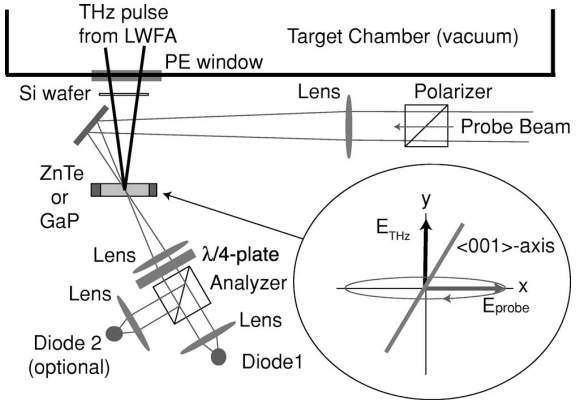

FIG. 6. Schematic representation of the setup for electro-optic sampling. If the $\lambda/4$ plate is used to transform the probe beam polarization to circular, then both diodes 1 and 2 are in operation (balanced detection). For linear or elliptical probe polarization, only diode 1 is operated. The inset shows the electric field vectors of the probe and THz pulse in relation to the crystal axis.

OAP2 (see Fig. 4) selects a specific polarization component which corresponds to vertical polarization at the crystal surface. Two types of EO crystals were used in these experiments; namely, ZnTe and GaP. Both crystals were 200 μm thick, free-standing, and cut in the $\langle 110 \rangle$ plane. For each crystal, the $\langle 001 \rangle$ axis was rotated to optimize the signal-to-noise ratio of the EOS measurement.

With future single-shot EOS experiments as a motivation, the single-diode detection (only diode 1 in operation) of the probe beam was applied on a more regular basis than balanced-diode detection.[34] With balanced EOS, both diodes are in operation and the probe beam is circularly polarized. Although the EO effect onto the probe beam is then small, the balancing allows for strong noise reduction. To resolve the sign of the THz pulse in the single-diode scheme,[38] the $\lambda/4$ plate was rotated to provide elliptical polarization. It has been shown[38] that in the sign-resolving single-diode configuration, the best signal-to-noise ratio is obtained with a small rotation of the $\lambda/4$ plate, such that near-zero optical transmission is realized. The THz wave will modify the probe beam ellipticity by a phase retardation $\Delta\phi$, and will cause an increase or decrease of the transmitted probe beam energy $T_{\mathrm{EO}}(\tau)$, depending on the sign of the THz field. For THz fields of equal but opposite magnitude, the change in transmission is not symmetric (not identical), but a well-known function of probe beam ellipticity.[38] For this reason each EOS transmission measurement $T_{\mathrm{EO}}(\tau)$ was symmetrized using this function, yielding the EOS signal $S_{\mathrm{EO}}(\tau)$.

There are several EOS-related effects that influence THz wave-form analysis.[36,39] (i) The probe beam has a finite pulse length, limiting the temporal resolution of the EOS method. (ii) Dispersion and absorption in the EO crystal causes THz pulse distortion. (iii) There is a mismatch between the phase velocity of the individual THz frequencies and the group velocity of the probe beam. Since both the ZnTe and GaP crystals have a well-characterized dispersion function in both the NIR and THz spectral domains,[36,40–42] these effects can be modeled and the original THz wave form $E_{\mathrm{THz}}(t)$ can be extracted from the measured (and symmetrized for probe beam ellipticity) EOS signal $S_{\mathrm{EO}}(\tau)$. In the frequency domain, a slowly varying envelope approximation can be applied to the convolution of the probe beam and the THz wave form,[39] yielding

$$S_{\mathrm{EO}}(\omega) \propto r_{41}(\omega) I_{\mathrm{pr}}(\omega) E_{\mathrm{THz}}(\omega) T_{\mathrm{crystal}}(\omega), \tag{7}$$

with $\omega = 2\pi\nu$ the angular frequency, $I_{\mathrm{pr}}(\omega) = e^{-\omega^2 \sigma_{\mathrm{pr}}^2/4}$, σ_{pr} the probe beam pulse length (rms), and $r_{41}(\omega)$ the EO coefficient. The crystal transfer function $T_{\mathrm{crystal}}(\omega)$ incorporates the dispersion, absorption, and mismatch in the EO crystal. For both crystals the transfer function is plotted in the inset of Fig. 7. Although the EO effect is larger for 200 μm thick ZnTe, its spectral resolution is limited to 4 THz (compared to 8 THz for 200 μm thick GaP). The spectral cutoff for both crystals can be attributed to velocity mismatch between probe and THz beam. Also plotted in the inset of Fig. 7 (see dotted curve) is the CTR spectrum of a 50 fs (rms) Gaussian electron beam (plasma radius of $\rho = 150$ μm at $\theta = 0.3$ rad). The EOS signal modeled from such a CTR pulse is shown in the main plot of Fig. 7 for ZnTe (dashed curve) and GaP (solid curve). Due to the spectral cutoff of ZnTe, multiple oscillations in the dashed curve are observed.

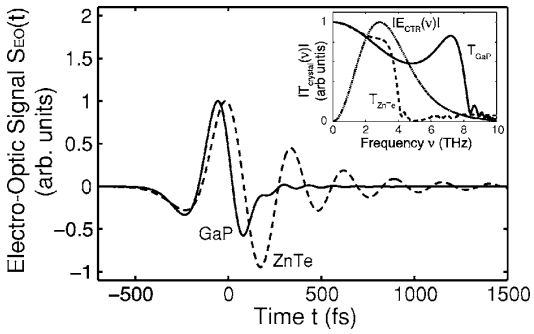

FIG. 7. The inset displays the crystal transfer functions $|T_{\mathrm{ZnTe}}(\nu)|$ (dashed curve) and $|T_{\mathrm{GaP}}(\nu)|$ (solid curve), as well as the CTR spectrum $|E_{\mathrm{CTR}}(\nu)|$ (dotted curve) from a 50 fs (rms) electron bunch. The corresponding EOS signal $S_{\mathrm{EO}}(\tau)$ is plotted for both crystals in the main plot.

B. Experimental results for electro-optic sampling

Several EOS scans under different experimental conditions were performed. The data (gray circles) in both images (a) and (b) in Fig. 8 are taken after rotation of the $\lambda/4$ plate by 5° and 45° (to circular polarization), respectively. In the latter case balanced diode detection was applied. Each data point represents an average of 30 shots, taken at 0.5 Hz repetition rate. The signal-to-noise ratios are of the same order; in the case of balanced detection, the noise could not be further reduced due to accelerator-related electronic background noise on the diodes. In both cases the EOS transmission data $T_{\mathrm{EO}}(\tau)$ was renormalized to take the probe beam ellipticity into account, yielding $S_{\mathrm{EO}}(\tau)$. Note that the detection of the coherent signals in Fig. 8 demonstrates the excellent shot-to-shot stability of bunch parameters that are critical to THz emission and detection (total charge, bunch length, and temporal synchronization). The Fourier transforms of the scans are plotted in each inset. All plots of Fig. 8 also contain modeled data based on (dashed curves) $S_{\mathrm{EO}}(\tau)$ from a single 50 fs (rms) electron bunch (and therefore a single THz pulse) and based on (solid curves) $S_{\mathrm{EO}}(\tau)$ from a double-pulse THz profile. Parameters for the double-pulse THz profile in Fig. 8(a) are a pulse separation of 230 fs, a relative field amplitude of 43% for the leading pulse, with each pulse based on CTR from a bunch with 50 fs (rms) length. The parameters for the double-pulse THz profile in Fig. 8(b) area 230 fs pulse separation, a relative field amplitude of 28% for the leading pulse, with each pulse based on CTR from a 70 fs (rms) bunch.

Another EOS dataset was taken using the GaP crystal. Figure 9 displays the measured data $T_{\mathrm{EO}}(\tau)$ (gray circles), without a $\lambda/4$ plate in the probe beam path. Each data point represents an average of 20 shots, taken at 1 Hz repetition rate. Due to residual birefringence (equivalent to $1.8^\circ \lambda/4$ plate rotation) in the GaP, the effective probe beam polarization was near-linear (small degree of ellipticity), and sign-resolved information was therefore still available. However,

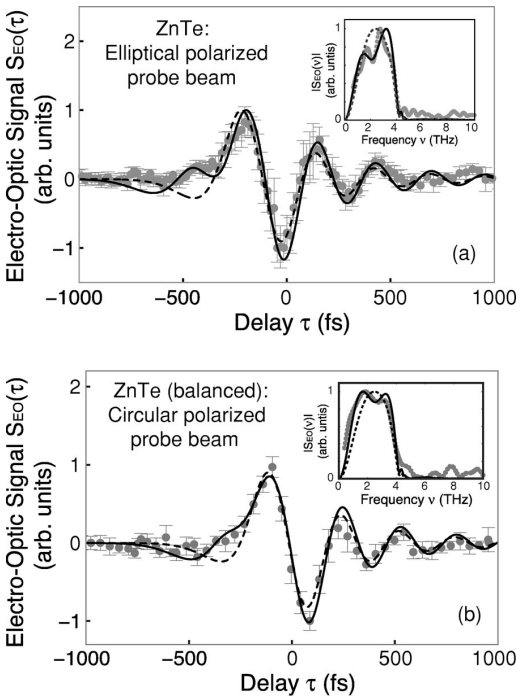

FIG. 8. ZnTe-based EOS wave forms $S_{EO}(\tau)$ (gray circles) measured with an elliptical polarized probe beam (a), and measured with a circular polarized probe beam in the balanced-diode scheme (b). The insets show the data in the Fourier domain $|S_{EO}(\nu)|$. The curves in all plots represent the modeled EOS signal of (dashed curves) THz radiation emitted by a single 50 fs (rms) bunch (single THz pulse), and of (solid curves) double-pulsed THz radiation. The two THz pulses are separated by 230 fs, and are both based on a 50 fs (rms) bunch.

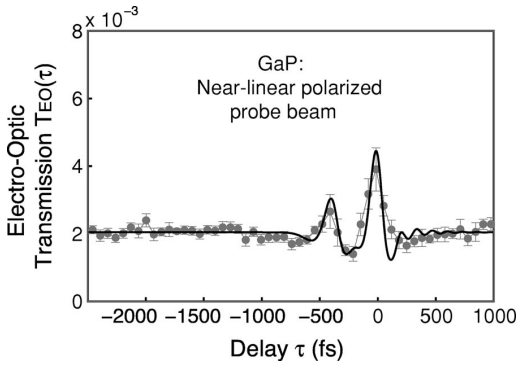

FIG. 9. EOS data $T_{EO}(\tau)$ (gray circles), taken at near-linear probe beam polarization with GaP. A modeled EOS profile based on double-pulsed THz radiation is displayed as the solid curve. For the model, the pulses were separated by 195 fs, with the leading pulse having a 50% relative field amplitude. Each THz pulse was calculated from a 50 fs (rms) bunch.

since the polarization state was so close to linear, the data was not renormalized to $S_{EO}(\tau)$ to take the ellipticity into account. It is for this reason that spectral analysis of the data is omitted. Instead, the modeled EOS wave form was modified to take the ellipticity into account. The GaP data (with up to 8 THz spectral resolution, and limited dispersion) unambiguously indicates that two THz pulses were produced. The modeled transmission signal (solid curve in Fig. 9) is based on a double-pulse THz profile, where the pulses are separated by 195 fs, with a 50% relative field amplitude of the leading pulse. Both THz pulses are calculated from a 50 fs (rms) bunch.

V. DISCUSSION OF THE RESULTS AND MODELS

The ensemble of data presented in this paper allows for analysis of the charge profile and bunch structure of SM-LWFA-produced electron bunches. Two ZnTe-based datasets (cf. Fig. 8) provided sign-resolved information of the THz radiation. Frequencies up to the 4 THz detection limit of the 200 μm thick ZnTe crystal were observed. Comparing the data to a model allows for the conclusion that sub-50 fs structure is present in the SM-LWFA-produced electron bunch. The bunch structure could be shorter, but the mismatch-dominated ZnTe would not be able to resolve the higher frequency components. However, assuming a longer bunch structure would significantly disagree with the measured spectral intensity in the 3–4 THz range. Also note that the measured bunch profile at the end of the plasma ramp (THz emission plane) is probably longer (via ballistic debunching due to the large momentum spread) than if measured at a position deeper into the plasma. The observed spectral oscillation (insets in Fig. 8), as well as the discrepancy between field measurements and the single-THz-pulse-based fit (main plots in Fig. 8), indicate that a more complex THz profile exists in the focal volume. A double-pulse-based model, with a pulse separation of $\simeq$230 fs and the leading pulse approximately having a 33% relative field amplitude, results in an improved temporal fit, and reproduces the spectral oscillation. Each THz pulse was calculated from a 50 fs (rms) Gaussian electron bunch.

The SCS experiment is suited for THz-to-laser synchronization and for indication of THz pulse and electron bunch length (and not well-suited for detailed bunch analysis). Comparison between data (cf. Fig. 5) and a model based on a double-pulse THz profile [two pulses each based on a 50 fs (rms) bunch, separated by 300 fs, with a 50% relative field amplitude for the leading bunch] indicates agreement, although the same is true for CTR from a single longer [400 fs (rms)] THz pulse. Note that this longer-single-pulse-based model is contradictory to the measured existence of coherent radiation above 3 THz, as measured independently in Ref. 10 and through EOS (cf. Sec. IV B). Overall, although temporal resolution is limited, the SCS measurements are consistent with a more complex THz profile in the focal volume.

The EOS data (cf. Fig. 9) taken with the 200 μm thick GaP crystal (up to 8 THz resolution) provided again a confirmation of the production of a more complex THz profile (suggesting a double-pulse profile). Since the experiment was operated at near-linear polarization, full temporal and spectral analysis was not possible. However, the measured profile (two positive peaks separated by 195 fs) unambiguously support the presence of two THz pulses in the focal volume. A modeled transmission curve based on a 195-fs-

separated double pulse, with the leading pulse having a 50% relative field amplitude, is in agreement with the data.

To model the EOS data of Figs. 8 and 9, we have considered bunch profiles other than the Gaussian profile, such as asymmetric bunches with a sharp rise and long tail. However, such considerations did not match the results, mainly due to the absence (in the model) of a spectral oscillation and a double THz pulse. The double pulse could be related to the LWFA-production of two bunches, since mechanisms such as plasma-gradient-induced wave breaking[43,44] and nonlinear transverse wave breaking[45] can result in a secondary stage of charge trapping. However, it is more likely that the double-pulse THz profile is a feature of spatio-temporal effects related to imperfections in the THz imaging beam line. Coma, diffraction, and other aberrations, can have a strong effect on the spatio-temporal profile of broad-bandwidth ultrashort optical wave forms.[46–48] For example, coma will result in the appearance of a multipulse profile in both the temporal and spatial domains. Future single-shot EOS experiments will aim at providing more insight into the detailed THz profile from the SM-LWFA-produced electron bunch, and the spatio-temporal coupling.

VI. SUMMARY AND CONCLUSION

We have reported on femtosecond bunch characterization of laser-plasma-produced electrons (SM-LWFA) by relying on the emission of CTR at the plasma-vacuum interface. Data taken with a semiconductor switching technique proved useful for THz and probe synchronization, and indicated a $<$400 fs THz envelope. A second technique, electro-optic sampling, allowed for measurement of the amplitude and phase of the THz wave form. THz frequencies up to the 200 μm thick ZnTe detection limit of 4 THz were resolved. The multishot nature of the experiment required and proved excellent SM-LWFA stability in terms of bunch parameters that are critical to THz emission and detection such as total charge, bunch length, and temporal synchronization. This stability is crucial for possible future pump-probe experiments. Comparison between data and a model demonstrated the production of sub-50 fs bunch structure. Detailed analysis, in combination with EOS data from a 200 μm thick GaP crystal (spectral response up to 8 THz), did indicate the production of a double-pulse THz profile in the focal volume, with both pulses separated by $\simeq$200–300 fs, and with the leading pulse having a 25%–45% relative field amplitude. In the models, both (CTR) pulses were derived from electron bunches with 50 fs (rms) bunch length. We suggest the double-pulse THz profile is likely related to the spatio-temporal profile of ultrashort electromagnetic pulses in an imperfect optical imaging system. We anticipate that future single-shot characterization of THz pulses will provide more insight into the detailed THz pulse and electron-bunch profile.

ACKNOWLEDGMENTS

The authors gratefully acknowledge contributions from J. M. Byrd, R. Huber, R. A. Kaindl, M. C. Martin, and Z. Hao on THz detection. This work was supported by the Director, Office of Science, Office of High Energy Physics, of the U.S. Department of Energy under Contract No. DE-AC02-05CH11231.

[1] T. Tajima and J. M. Dawson, Phys. Rev. Lett. **43**, 267 (1979).
[2] E. Esarey, P. Sprangle, J. Krall, and A. Ting, IEEE Trans. Plasma Sci. **24**, 252 (1996).
[3] A. Modena, Z. Najmudin, A. E. Dangor, C. E. Clayton, K. A. Marsh, C. Joshi, V. Malka, C. B. Darrow, C. Danson, D. Neely *et al.*, Nature (London) **377**, 606 (1995).
[4] A. Ting, C. I. Moore, K. Krushelnick, C. Manka, E. Esarey, P. Sprangle, R. Hubbard, H. R. Burris, R. Fischer, and M. Baine, Phys. Plasmas **4**, 1889 (1997).
[5] V. Malka, S. Fritzler, E. Lefebvre, M.-M. Aleonard, F. Burgy, J.-P. Chambaret, J.-F. Chemin, K. Krushelnick, G. Malka, S. P. D. Mangles *et al.*, Science **298**, 1596 (2002).
[6] W. P. Leemans, P. Catravas, E. Esarey, C. G. R. Geddes, C. Toth, R. Trines, C. B. Schroeder, B. A. Shadwick, J. van Tilborg, and J. Faure, Phys. Rev. Lett. **89**, 174802 (2002).
[7] S. P. D. Mangles, C. D. Murphy, Z. Najmudin, A. G. R. Thomas, J. L. Collier, A. E. Dangor, E. J. Divall, P. S. Foster, J. G. Gallacher, C. J. Hooker *et al.*, Nature (London) **431**, 535 (2004).
[8] C. G. R. Geddes, Cs. Tóth, J. van Tilborg, E. Esarey, C. B. Schroeder, D. Bruhwiler, C. Nieter, J. Cary, and W. P. Leemans, Nature (London) **431**, 538 (2004).
[9] J. Faure, Y. Glinec, A. Pukhov, S. Kiselev, S. Gordienko, E. Lefebvre, J.-P. Rousseau, F. Burgy, and V. Malka, Nature (London) **431**, 541 (2004).
[10] W. P. Leemans, C. G. R. Geddes, J. Faure, Cs. Tóth, J. van Tilborg, C. B. Schroeder, E. Esarey, G. Fubiani, D. Auerbach, B. Marcelis *et al.*, Phys. Rev. Lett. **91**, 074802 (2003).
[11] C. B. Schroeder, E. Esarey, J. van Tilborg, and W. P. Leemans, Phys. Rev. E **69**, 016501 (2004).
[12] W. P. Leemans, J. van Tilborg, J. Faure, C. G. R. Geddes, Cs. Tóth, C. B. Schroeder, E. Esarey, G. Fubiani, and G. Dugan, Phys. Plasmas **11**, 2899 (2004).
[13] J. van Tilborg, C. B. Schroeder, E. Esarey, and W. P. Leemans, Laser Part. Beams **22**, 415 (2004).
[14] J. van Tilborg, C. B. Schroeder, C. V. Filip, Cs. Tóth, C. G. R. Geddes, G. Fubiani, R. Huber, R. A. Kaindl, E. Esarey, and W. P. Leemans, Phys. Rev. Lett. **96**, 014801 (2006).
[15] P. Catravas, E. Esarey, and W. P. Leemans, Meas. Sci. Technol. **12**, 1828 (2001).
[16] E. Esarey, B. A. Shadwick, P. Catravas, and W. P. Leemans, Phys. Rev. E **65**, 056505 (2002).
[17] A. Rousse, K. T. Phuoc, R. Shah, A. Pukhov, E. Lefebvre, V. Malka, S. Kiselev, F. Burgy, J.-P. Rousseau, D. Umstadter *et al.*, Phys. Rev. Lett. **93**, 135005 (2004).
[18] W. P. Leemans, D. Rodgers, P. E. Catravas, C. G. R. Geddes, G. Fubiani, E. Esarey, B. A. Shadwick, R. Donahue, and A. Smith, Phys. Plasmas **8**, 2510 (2001).
[19] K.-C. Tzeng, W. B. Mori, and T. Katsouleas, Phys. Rev. Lett. **79**, 5258 (1997).
[20] E. Esarey, B. Hafizi, R. Hubbard, and A. Ting, Phys. Rev. Lett. **80**, 5552 (1998).
[21] S. Banerjee, S. Sepke, R. Shah, A. Valenzuela, A. Maksimchuk, and D. Umstadter, Phys. Rev. Lett. **95**, 035004 (2005).
[22] X. Yan, A. M. MacLeod, W. A. Gillespie, G. M. H. Knippels, D. Oepts, A. F. G. van der Meer, and W. Seidel, Phys. Rev. Lett. **85**, 3404 (2000).
[23] M. J. Fitch, A. C. Melissinos, P. L. Colestock, J.-P. Carneiro, H. T. Edwards, and W. H. Hartung, Phys. Rev. Lett. **87**, 034801 (2001).
[24] I. Wilke, A. M. MacLeod, W. A. Gillespie, G. Berden, G. M. H. Knippels, and A. F. G. van der Meer, Phys. Rev. Lett. **88**, 124801 (2002).
[25] G. Berden, S. P. Jamison, A. M. MacLeod, W. A. Gillespie, B. Redlich, and A. F. G. van der Meer, Phys. Rev. Lett. **93**, 114802 (2004).
[26] A. L. Cavalieri, D. M. Fritz, S. H. Lee, P. H. Bucksbaum, D. A. Reis, J. Rudati, D. M. Mills, P. H. Fuoss, G. B. Stephenson, C. C. Kao *et al.*, Phys. Rev. Lett. **94**, 114801 (2005).
[27] U. Happek, A. J. Sievers, and E. B. Blum, Phys. Rev. Lett. **67**, 2962 (1991).
[28] Y. Shibata, T. Takahashi, T. Kanai, K. Ishi, M. Ikezawa, J. Ohkuma, S. Okuda, and T. Okada, Phys. Rev. E **50**, 1479 (1994).
[29] P. Kung, H.-C. Lihn, H. Wiedemann, and D. Bocek, Phys. Rev. Lett. **73**, 967 (1994).

[30] M. L. Ter-Mikaelian, *High-Energy Electromagnetic Processes in Condensed Media* (Wiley, New York, 1972).
[31] A. J. Alcock and P. B. Corkum, Can. J. Phys. **57**, 1280 (1979).
[32] P. B. Corkum, IEEE J. Quantum Electron. **21**, 216 (1985).
[33] C. Rolland and P. B. Corkum, J. Opt. Soc. Am. B **3**, 1625 (1986).
[34] J. A. Valdmanis, G. Mourou, and C. W. Gabel, Appl. Phys. Lett. **41**, 211 (1982).
[35] A. Yariv, *Quantum Electronics* (Wiley, New York, 1988).
[36] J. Faure, J. van Tilborg, R. A. Kaindl, and W. P. Leemans, Opt. Quantum Electron. **36**, 681 (2004).
[37] J. V. Lepore and R. J. Riddell, Jr., Phys. Rev. D **13**, 2300 (1976).
[38] Z. Jiang, F. G. Sun, Q. Chen, and X.-C. Zhang, Appl. Phys. Lett. **74**, 1191 (1999).
[39] G. Gallot and D. Grischkowsky, J. Opt. Soc. Am. B **16**, 1204 (1999).
[40] A. S. Barker Jr., Phys. Rev. **165**, 917 (1968).
[41] G. Gallot, J. Zhang, R. W. McGowan, Tae-In Jeon, and D. Grischkowsky, Appl. Phys. Lett. **74**, 3450 (1999).
[42] D. T. F. Marple, J. Appl. Phys. **35**, 539 (1964).
[43] S. Bulanov, N. Naumova, F. Pegoraro, and J. Sakai, Phys. Rev. E **58**, R5257 (1998).
[44] P. Tomassini, M. Galimberti, A. Giulietti, D. Giulietti, L. A. Gizzi, L. Labate, and F. Pegoraro, Phys. Rev. ST Accel. Beams **6**, 121301 (2003).
[45] S. V. Bulanov, F. Pegoraro, A. M. Pukhov, and A. S. Sakharov, Phys. Rev. Lett. **78**, 4205 (1997).
[46] S. Hunsche, S. Feng, H. G. Winful, A. Leitenstorfer, M. C. Nuss, and E. P. Ippen, J. Opt. Soc. Am. A **16**, 2025 (1999).
[47] Z. L. Horváth and Zs. Bor, Phys. Rev. E **63**, 026601 (2001).
[48] U. Fuchs, U. D. Zeitner, and A. Tünnermann, Opt. Express **13**, 3852 (2005).